

Highlights

Defect detection in glass fabric reinforced thermoplastics by laboratory-based X-ray scattering

Özgül Öztürk, Rolf Brönnimann, Peter Modregger

- X-ray transmission and scattering signals are anti-correlated for GFRT samples
- Local fiber shifts defects in GFRT can be detected by X-ray transmission and scattering
- Defects are detectable in the hidden glass fiber layer

Defect detection in glass fabric reinforced thermoplastics by laboratory-based X-ray scattering

Özgül Öztürk^{a,*}, Rolf Brönnimann^b and Peter Modregger^{a,c,**}

^aPhysics Department, University of Siegen, Walter-Flex-Str. 3, Siegen, 57072, Germany

^bEmpa, Swiss Federal Laboratories for Materials Science and Technology, Dübendorf, 8600, Switzerland

^cCenter for X-ray and Nano Science, Deutsches Elektronen-Synchrotron, Hamburg, 22607, Germany

ARTICLE INFO

Keywords:

D. Non-destructive testing
A. Polymer-matrix composites (PMCs)
B. Defects
D. X-ray scattering

ABSTRACT

Glass fabric reinforced thermoplastic (GFRT) constitutes a class of composite materials that are especially suited for automobile construction due to their combination of low weight, ease of production and mechanical properties. However, in the manufacturing process, during forming of prefabricated laminates, defects in the glass fabric as well as in the polymer matrix can occur, which may compromise the safety or the lifetime of components. Thus, the detection of defects in GFRTs for production monitoring and a deep understanding of defect formation/evolution is essential for mass production. Here, we experimentally demonstrate that a certain type of defect (i.e., local fiber shifts), can be detected reliably by X-ray scattering based on the edge-illumination principle. This implies applications for research on mechanism of defect formation as well as for industrial application in production monitoring.

Introduction

Lightweight composite materials have attracted ever increasing attention from researchers and from the manufacturing industry in recent decades. Their unique combination of properties such as high strength to weight ratio, resistance to corrosion and economical manufacturing render them suitable for applications such as aerospace, automobiles or construction [1]. A class of composite materials are fiber reinforced polymers, which are generally comprised of several fiber layers (e.g., glass, carbon or aramid) nested in a polymer matrix (e.g., thermoplastic, epoxy or vinyl ester) [2]. Each of these material systems has their own unique mechanical properties and area of application [3].

Glass fabric reinforced thermoplastics (GFRT) are especially suitable for automobile manufacturing due to its ease of production, high stiffness, corrosion resistance and recyclability [4]. Naturally, one of the main objectives of substituting metallic components by GFRT is weight reduction, which leads to reduced fuel consumption and ultimately reduced CO₂ emissions. Furthermore, GFRT components can be produced by conventional forming presses from ready-made, prefabricated laminates, which is comparatively cost efficient. However, defects in the glass fabric or the thermoplastic matrix can be created or enlarged during forming, which poses a serious safety concern for structural components [5, 6]. Therefore, various non-destructive testing (NDT) techniques are investigated for the understanding of defect formation and evolution as well as for the application in production monitoring of GFRT components [7]. Examples for NDT techniques applied to composite materials

include ultrasonic imaging [8, 9], THz imaging [10, 11, 12], X-ray computed tomography [11] or infrared thermography [13].

In addition, laboratory-based X-ray scattering based on the edge-illumination (EI) principle was applied to defect detection in composite materials [14]. EI constitutes a phase-sensitive X-ray imaging technique that simultaneously provides absorption, phase and scattering contrast [15, 16, 17]. The principle of image formation can be described as follows (Fig. 1a). The incident X-ray beam is split into smaller beamlets by an apertured sample mask. The beamlets are distorted by the interaction with the sample downstream. These distortions are then analyzed by an apertured detector mask and measured by a pixelated detector. The pitch of the apertures projected onto the detector matches the pixel size and, thus, one sample mask aperture and one detector mask aperture contribute to the signal in a given detector pixel column. In the experiment, the sample mask is laterally scanned by a fraction of its pitch, which results in a Gaussian-like intensity distribution, called the illumination curve (IC), for each detector pixel (Fig. 1b). A complete data set contains a reference (i.e., flat-field) IC without a sample present in the beam and a sample IC. The aforementioned sample-induced distortions of the beamlets appear as specific differences between the flat-field and the sample IC: absorption reduces the height, refraction shifts the peak position and scattering is reflected in a broadening of the IC. EI constitutes an incoherent imaging system with typical aperture sizes of $>10\ \mu\text{m}$ rendering this setup insensitive to mechanical vibrations and compatible with standard laboratory-based X-ray sources.

In the context of defect detection in composite materials, the scattering contrast is of particular interest. Scattering originates from refraction at numerous microscopic sample inhomogeneities [18, 19] (e.g., glass-polymer interfaces), which cannot be resolved individually (Fig. 1 a - top view). Thus, the scattering contrast constitutes a measure of sample

*Corresponding author

**Principal corresponding author

✉ Oezguel.Oeztuerk@uni-siegen.de (Ö. Öztürk);

rolf.broennimann@empa.ch (R. Brönnimann);

peter.modregger@uni-siegen.de (P. Modregger)

ORCID(s):

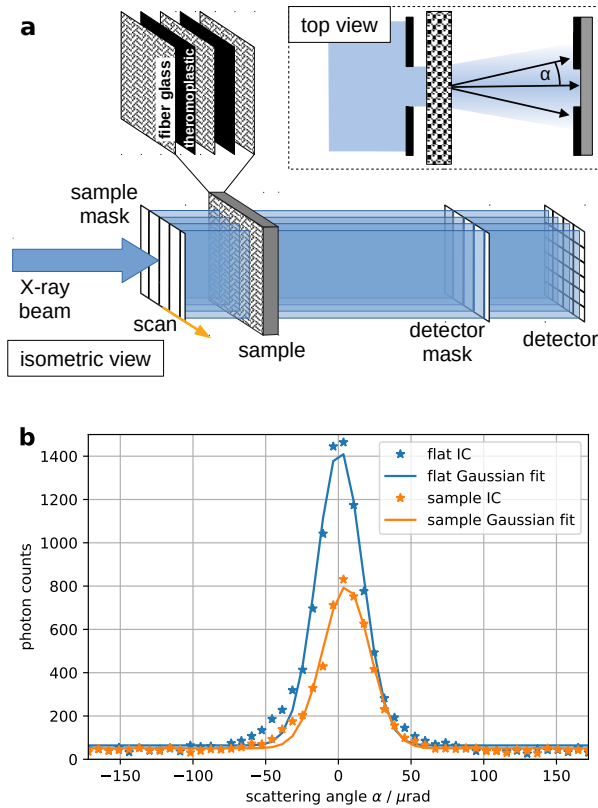


Figure 1: Principle of X-ray imaging with edge-illumination. (a) Sketch of the setup and the composite material system (GFRT). In the experiment, the sample mask is laterally scanned, which provides a Gaussian-like intensity signal, called the illumination curve, for each detector pixel as shown in (b). This panel shows the flat-field IC, measured without sample, and a sample IC, measured with a sample, for the same detector pixel. Intensity reduction is due to absorption, a shift in peak position is due to refraction and a broadening of the curve is due to sub-pixel scattering.

inhomogeneity within a detector pixel, which renders it a sub-pixel contrast that is complementary to the absorption and the refraction signal. For example, it has been demonstrated that the scattering contrast (and its higher orders) can be used to measure particle sizes down $8 \mu\text{m}$ with $250 \mu\text{m}$ pixels [20]. The sub-pixel nature of the scattering contrast opens the possibility for faster scans and/or dose reduction by exploiting larger pixel sizes. X-ray scattering was also combined with tomography revealing sample inhomogeneities in three dimensions [19]. Up to now, multi-modal X-ray imaging with EI was applied to the detection of impact damage in a carbon fibre/epoxy resin laminate in radiographic face-on geometry [14] as well as in tomographic edge-on geometry, which revealed delamination and cracks [21, 22], and to the characterization of porosity in face-on geometry for the same material system [23, 24].

The so-called dark-field contrast [25] provided by laboratory-based grating interferometry (GI) [26] is functionally equivalent to the scattering contrast accessible by EI [20]. Compared to EI, GI constitutes a coherent imaging system

that relies on the fractional Talbot effect (i.e., coherent Fresnel diffraction at periodic structures). The utilization of (partial) coherence implies the necessity for optical components with small structures (few micrometers), higher requirements for the X-ray source and the lack of contribution of parts of the spectrum to the dark-field signal [27]. Nevertheless, GI is actively utilized in the field of composite materials and examples include the differentiation of material phases in concrete [28], the visualization of delamination in carbon fibre reinforced plastic composites (CFRP) [29], the characterization of anisotropic fibre orientation in CFRP and short fiber GFRP [30, 31, 32], monitoring of bonded aircraft repairs in CRFP [33], the measurement of fiber length in short fiber composites [34], the characterization of fiber waviness in CFRP [35] as well as first investigations into quantitative interpretation [36]. Recently, it was also demonstrated that local microfiber orientation in full sized polymer-matrix composite components can be characterized by synchrotron radiation-based X-ray scattering tensor tomography [37], which is a variation of GI.

Defects in composite materials include delamination (i.e., separation of fiber layers), consolidation (i.e., variations of the polymer matrix thickness), local fiber shifts (i.e., local agglomeration of fibers in one layer leaving behind a hole in the fabric of this layer), global fiber shift (i.e., lateral offset of one fabric layer with respect to the others) or cracks (i.e., broken fibers in one or more fabric layer). For GFRT it has been demonstrated that delamination and consolidation can be detected by THz imaging [12]. In this study, we are aiming to provide a proof of concept for the detection of local fiber shifts in GFRT by means of X-ray scattering with EI. To this end, we will first describe the experimental setup and then describe the retrieval of the multi-modal contrasts from experimental images. Afterwards, we will show the absorption and scattering contrasts for 9 GFRT samples (3 control, 3 with a local fiber shift in the top layer and 3 with a local fiber shift in the middle layer) and establish an expected negative correlation between these contrasts. We will introduce the standard deviation of transmission and scattering signals over the field of view (FoV) as an observable for automatic defect detection. Finally, we will use a harmonic analysis of vertically averaged scattering signals in order to demonstrate a reliable detection of local fiber shifts in GFRT composites.

Experiment and contrast retrieval

The glass fabric of the GFRT samples were made from bi-directional twill 2/2 E-glass roving fiber, where the twill 2/2 indicates that two wrap yarns (horizontal fibers) travel over and under two weft yarns (vertical fibers) forming a diagonal pattern. Three glass fabric layers were incorporated in a thermoplastic polymer matrix (Fig. 1a) made of polypropylene (PP) and had a thickness of 1.5 mm. The samples were produced by Bond-Laminates, Lanxess Group (Brilon, Germany).

The laboratory-based experiment was carried out with a newly build EI set-up at the University of Siegen (Germany). The source was an XWT-160-SE X-ray tube (X-RAY WorX, Garbsen, Germany) with a tungsten target operated at 0.5 mA current and 40 kV voltage. While it is possible to increase the current, we have observed an unacceptable increase of source size for this tube. The X-ray detector was a Pilatus 3X 200 K-A (DECTRIS, Baden, Switzerland) with a Si absorber and a pixel size of 172 μm . Both masks were manufactured by laser ablation (EMPA, Dübendorf, Switzerland) of tungsten foil with a thickness of 150 μm (Goodfellow, Huntingdon, UK). The sample mask featured a pitch of 137.6 μm and line apertures sizes of 17.2 μm and was placed at 0.41 m away from the detector. The detector mask featured a pitch of 163.4 μm and line apertures sizes of 23 μm and was placed at 0.1 m upstream of the detector. The different pitches account for geometric magnification and provided projected pitches at the detector, which matched the pixel size. The sample to detector distance was 0.36 m and total setup length was 2.05 m. The FoV was limited by the size of the test masks to $(2 \times 1.7) \text{cm}^2$. This setup constituted a prototype utilizing the instrumentation at hand and can be significantly optimized (e.g., a more appropriate combination of X-ray source and detector).

In the experiment, the flat-field ICs were measured by scanning the sample mask over one period in 50 steps with an acquisition time of 50 s (Fig. 1b). The GFRT samples were oriented so that one weave is horizontal and the other is vertical in the detector image. Regions of interest were identified by standard absorption contrast (i.e., masks moved out of the X-ray beam) and then imaged at 50 IC positions using 16 dithering steps with (i.e., moving the sample in sub-pixel steps [38]) with a frame time of 3.125 s each. While dithering in EI is generally used to improve spatial resolution, here the corresponding frames were added up to improve the sub-pixel sampling of the composites. Thus, total acquisition time per sample IC step was 50 s and total scan time was about 90 min.

Retrieval of the multi-modal contrasts provided by EI involved a pixel-wise fit [39] of the measured flat-field IC and sample IC to a Gaussian function with an additional offset c

$$I_{f,s}(\alpha, x, y) = A_{f,s}(x, y) e^{-\frac{(\alpha - \mu_{f,s}(x,y))^2}{2\sigma_{f,s}^2(x,y)}} + c(x, y) \quad (1)$$

with α , the scattering angle (Fig. 1a - top view), (x, y) , the pixel position, $A_{f,s}(x, y)$, the height of the Gaussian, $\mu_{f,s}(x, y)$, the peak position, $\sigma_{f,s}^2(x, y)$, the width and the subscripts f and s designate the flat-field and sample ICs, respectively. Exemplary fitting results are shown in Fig. 1b. The offset $c(x, y)$ had an average value 5% of the peak over the FoV and was likely due to parasitic transmission through aperture edges or X-ray source tails. Finally, the transmission $t(x, y)$ was calculated according to

$$t(x, y) = \frac{A_s(x, y)}{A_f(x, y)}, \quad (2)$$

the refraction $\Delta\alpha$ (no images shown) according to

$$\Delta\alpha(x, y) = \mu_s(x, y) - \mu_f(x, y), \quad (3)$$

and the sub-pixel scattering signal according to

$$\sigma^2(x, y) = \sigma_s^2(x, y) - \sigma_f^2(x, y). \quad (4)$$

The resulting contrasts were 2×2 pixel binned to decrease variations over the FoV and resulting in an effective pixel size of 344 μm .

Defect detection

Figure 2 shows the measured transmission and scattering signals for 3 control samples (c1-c3; top row), 3 samples with a local fiber shift defect in the top fabric layer (d1-d3; middle row) and 3 samples with a local fiber shift defect in the (hidden) middle fabric layer (d4-d6; bottom row). The average transmission value of the control samples ($\bar{t}_c = 0.570 \pm 0.038$; interval is the standard deviation) did not differ significantly from the corresponding value of the defect samples ($\bar{t}_d = 0.579 \pm 0.061$). This indicates that the entire defective area was imaged as the total amount of glass fibers was constant and a partial measurement would lead to larger differences. While the same holds true for the scattering values ($\bar{\sigma}_c^2 = (28 \pm 11) \mu\text{rad}^2$ versus $\bar{\sigma}_d^2 = (34 \pm 13) \mu\text{rad}^2$), the latter showed a significantly larger relative variation within the FoV (the 'noisy' appearance of scattering images in Fig. 2). This is due to the fact that the width of a single glass fiber ($\approx 10 \mu\text{m}$) is comparable to the aperture of the sample mask (17.2 μm), which results in a strong dependency of the scattering signal on the specific fiber sections exposed to X-rays. In order to lessen the variations in the scattering signal, dithering was used during scanning and pixel binning for data analysis.

Local fiber shifts are visible in the transmission images (Fig. 2) as distortion of the weave pattern, when visually compared to the control samples. These distortions are also accompanied by an increased variation of transmission values over the FoV. While the latter also holds true for the scattering contrast, local fiber shifts also appear in this contrast as locally increased/decreased scattering values (i.e., increased oscillatory modulations), which outline the defect (especially noticeable for sample d1).

These observations were consistent with expectations. As stated above, local fiber shifts are local agglomerations of glass fibers in one layer, which leave behind a hole in the fabric of this layer. Since glass (modeled as SiO_2 with a density of 2.5 g/cm^3) has a much smaller absorption length (1.8 mm [40] at the mean photon energy of 20 keV) than the PP matrix (modeled as C_3H_6 with a density of 0.86 g/cm^3 ; absorption length is 71 mm [40] at 20 keV), an absence of glass fibers will increase transmission for an identical sample thickness and vice versa for the agglomeration of fibers. Since the scattering contrast originates from glass-PP interfaces, scattering values increase for fiber agglomerations and decrease for absent fibers. These effects are

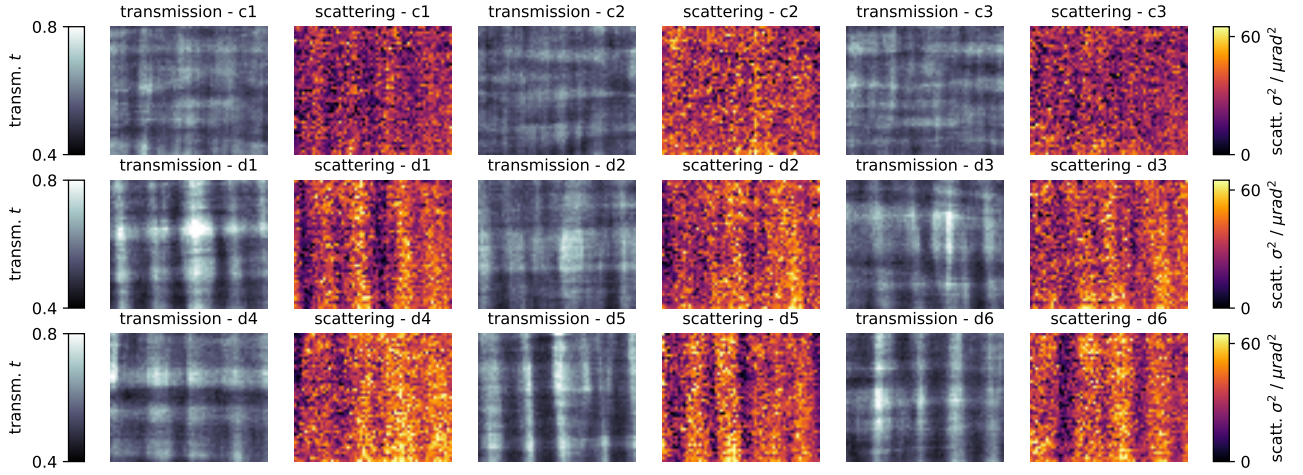


Figure 2: Transmission and scattering contrasts of 9 GFRT samples. All transmission (scattering) images share the same colormap as indicated on the left (on the right) and a FoV of $(2 \times 1.7) \text{ cm}^2$ is shown. Top row are the control samples (c1-c3), middle row are the samples with a local fiber shift defect in the top glass fabric layer (d1-d3) and bottom row are the samples with a local fiber shift defect in the middle glass fabric layer (d4-d6).

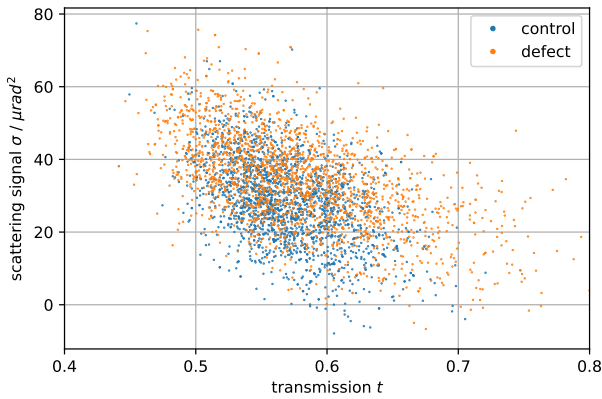


Figure 3: Scatter plot of transmission t and scattering values σ^2 of 4000 pixels randomly selected from control and defect samples, respectively. The transmission values are negatively correlated ($r = -0.52$) with the scattering values.

noticeable in Fig. 2. This explanation is confirmed by the scatter plot of transmission versus scattering values for 4000 randomly selected pixels from all 9 scans shown in Fig. 3. A clear negative correlation ($r = -0.52$) using all available pixels between the transmission values (e.g., low for fiber agglomerations) and scattering values (e.g., high for fiber agglomerations) demonstrates the agreement.

In the following, we investigated two procedures for automatic defect detection with an application in production monitoring in mind.

First, we exploited the difference in contrast variations between the control and the defective samples. To this end, we used the standard deviation of the 2 contrasts over the FoV as the observable, which is similar to the utilization of the refraction contrast for porosity determination in [24]. Figure 4 displays the individual standard deviations for

the transmission (a) and scattering (b) contrast. We used a two-sided t-test [41] for the determination of statistical significance of the difference between group means and the contrast to noise ration (CNR), given by

$$\text{CNR} = \frac{\bar{h}_1 - \bar{h}_2}{\sqrt{\text{var}(h_1)^2 + \text{var}(h_2)}} \quad (5)$$

with $\bar{h}_{1,2}$ the mean of group 1 and 2 and $\text{var}(h_{1,2})$ the corresponding variance, as a measure of effect size.

The results are included in Fig. 4, which demonstrate a statistical significant difference between the group means for both contrasts and a robust CNR of 3.0 for the standard deviation of the transmission and of 2.1 for the standard deviation of the scattering contrast. Please note that the defects in the middle layer (samples d4-d6), which are not visually accessible, were as detectable as the defects in the top layer (samples d1-d3). Naturally, the measured standard deviation values depend on the employed FoV. Increasing the FoV for the defective samples to non-defective regions would lower the difference between control and defective observables. However, this can be readily addressed by utilizing a moving image section of appropriate size and highlighting regions of increased standard deviations as potential defects.

Further, taking these results naively at face value one might come to the conclusion that the transmission contrast is superior to the scattering contrast for defect detection. However, using the standard deviation of the transmission contrast as the observable for detection of local fiber shifts implicitly assumes a constant sample thickness as variations in the thickness (i.e., consolidation) could also account for variations in the transmission. In fact, without using the *a priori* knowledge that the sample thickness is indeed constant, only the scattering signal may reveal a local agglomeration or absent of glass fibers. Thus, the combination

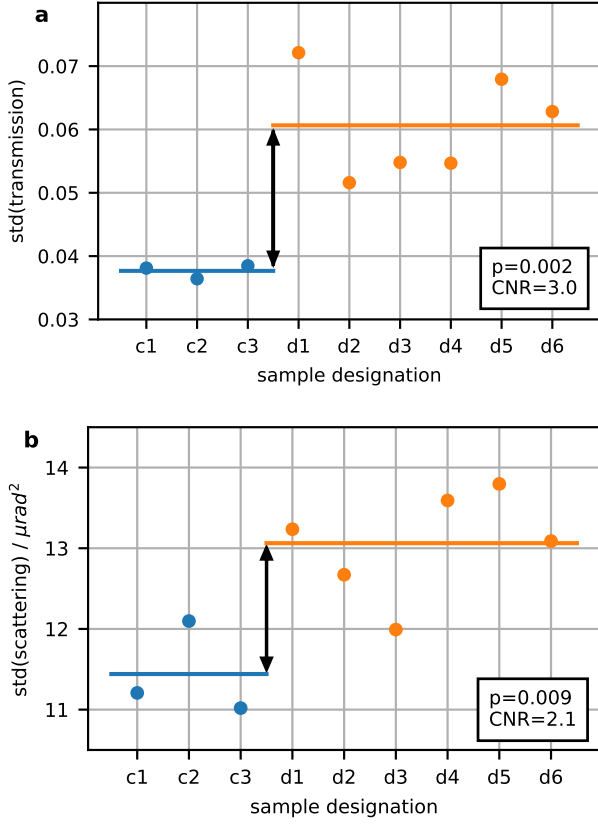


Figure 4: The standard deviations of transmission (a) and scattering signals (b) over the FoV in Fig. 2 show a statistically significant difference between control and defect groups for both contrasts. Horizontal lines are group averages.

of transmission and scattering contrast has the potential to detect and to distinguish local fiber shifts and consolidation.

For the reasons laid out above, the second procedure for automatic defect detection investigated used the scattering contrast only. Here, we used a harmonic analysis of the contrast, which suggested itself by the periodic nature of the glass fabric. First, we calculated the vertically averaged scattering values $\tilde{\sigma}(x_i)$ for the horizontal pixel position x_i by

$$\tilde{\sigma}^2(x_i) = \sum_j \sigma^2(y_j, x_i) / N_y \quad (6)$$

with y_j , the vertical pixel position and N_y the number of pixels in vertical direction. This vertical averaging for increasing the signal is justified by the fact that only horizontal scattering can be observed, which leads to the tendency for vertical features in the scattering contrast (see Fig. 2). As long as the fiber fabric is roughly oriented along the horizontal/vertical image axes, vertical averaging can be used to increase the signal.

Two examples (1 control and 1 defect sample) for vertically averaged scattering values are displayed in Fig. 5a, which also illustrates the principle of harmonic analysis [42]. The cosines associated with the 4th harmonic, which reflects

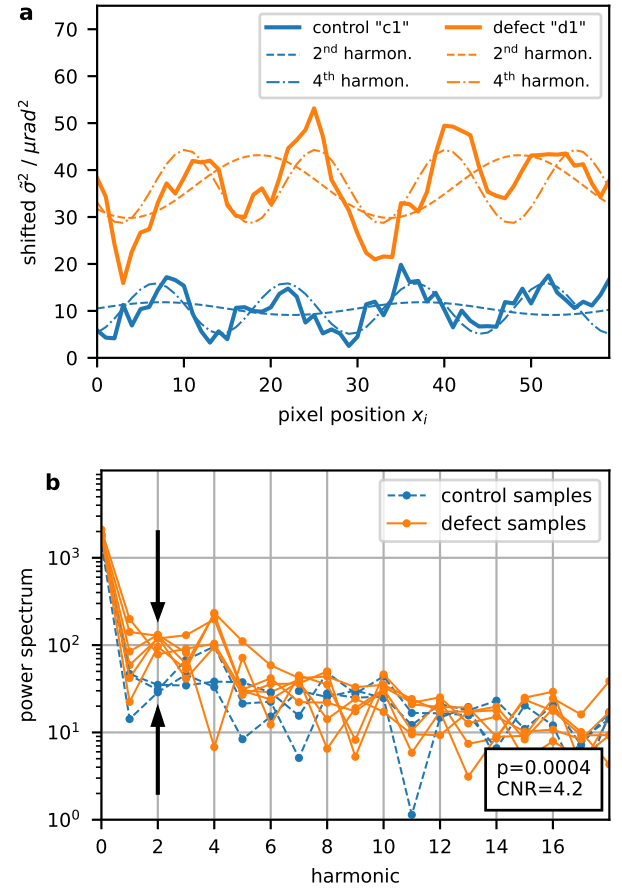


Figure 5: Improved defect detection with scattering. (a) Vertically averaged scattering signals σ^2 (continuous lines) of control sample 'c1' and defect sample 'd1'. The curves have been shifted for clarity. Dashed lines are cosines corresponding to the 2nd and 4th harmonics of each vertically averaged scattering signal. The 4th harmonic reproduces the periodicity of the glass fiber fabric, while the 2nd harmonic (small amplitude for 'c1'; large amplitude for 'd1') is used for defect detection. (b) The power spectra of vertically averaged scattering signals of all samples. A clear distinction in the 2nd harmonic between the control and the defect groups is visible.

the periodicity of the signal, and the cosines associated with the 2nd harmonic, which will be used as the observable for defect detection, are shown. As discussed above, a local fiber shift defect increases the scattering signal at the edges of the defect and decreases this contrast in the middle. This is reflected by an increase of the scattering modulation around the defect, which then increases the strength of the 4th harmonic.

Panel 5b shows the power spectra of the vertically averaged scattering values, which were calculated by numerical Fourier transform. Looking at the 2nd harmonic it is evident that the control and the defect group can be readily distinguished. Statistical analysis as above revealed that the CNR is 4.2 (with p=0.0004), which strongly suggests that the scattering signal can be used for a reliable detection of local fiber shift defects in GFRT composite materials. A similar

harmonic analysis of the transmission contrasts (not shown) did not lead to any improvement for defect detection.

Conclusion and outlook

We have demonstrated that local fiber shifts in GFRT composites can be reliably detected by laboratory-based EI. We have used a face-on sample geometry for radiographic imaging, which lends well to an application in production monitoring as it is independent from lateral sample sizes. We have introduced the standard deviations over the FoV for the transmission and scattering contrasts as an observable for automatic defect detection and found a robust differentiation between control and defective samples. The CNR between those groups was 3.0 or for the transmission contrast and 2.1 for the scattering contrast. Local fiber shift in the hidden middle layer were as detectable as in the top layer of the GFRT samples. We discussed that the scattering contrast depends only on the number of glass-PP interfaces within a pixel, which renders this contrast significantly less sensitive to total sample thickness (e.g., by consolidation) than the transmission contrast. Further, we have capitalized on the periodicity of the glass fabric and used a harmonic analysis of the vertically averaged scattering signals as an alternative observable. This resulted in an increased CNR between control and defective samples of 4.2. These findings strongly suggest the application of X-ray scattering for research on mechanism of defect formation in composite materials as well as for industrial application in production monitoring.

The study was conducted with a prototype EI setup that can be significantly improved with respect to measurement time and strength of retrieved signals. For example, X-ray tubes of higher power without compromising the source size are available, which in combination with a CdTe-based X-ray detector, would significantly decrease scan times. The scattering signal can be maximized by optimizing aperture sizes of the masks for the application at hand. Finally, measurement times can be further decrease by utilizing a single shot approach, which images the sample on the highly sensitive slope of the ICs and eliminates the necessity for scanning.

Declaration of competing interest

The authors have no competing interest to declare.

Acknowledgements

Ö. Öztürk acknowledges funding by DFG GU 535/6 – 1. We would like to thank Matthias Kahl, Aya Souliman and Peter Haring Bolívar (Institute for High Frequency and Quantum Electronics, University of Siegen, Germany), Bernd Engel (Institute for Production Engineering, University of Siegen, Germany) and Bond-Laminates, a company of the LANXESS Group, for providing samples and reference measurements, and for fruitful discussions.

CRedit authorship contribution statement

Özgül Öztürk: Data curation, Investigation, Writing - review & editing. **Rolf Brönnimann:** Resources, Methodology, Writing - review & editing. **Peter Modregger:** Conceptualization, Formal analysis, Supervision, Visualization, Writing - original draft.

References

- [1] D. K. Rajak, D. D. Pagar, R. Kumar, C. I. Pruncu, Recent progress of reinforcement materials: A comprehensive overview of composite materials, *J. Mater. Res. Technol.* 8 (2019) 6354–6374.
- [2] M. A. Masuelli, Introduction of Fibre-Reinforced Polymers - Polymers and Composites: Concepts, Properties and Processes, in: M. A. Masuelli (Ed.), *Fiber Reinf. Polym.*, IntechOpen, Rijeka, 2013.
- [3] M. O. Seydibeyoglu, A. K. Mohanty, M. Misra, *Fiber technology for fiber-reinforced composites*, Woodhead Publishing, 2017.
- [4] J. Fan, J. Njuguna, An introduction to lightweight composite materials and their use in transport structures, in: J. Njuguna (Ed.), *Light. Compos. Struct. Transp.*, Woodhead Publishing, 2016, pp. 3–34.
- [5] M. Berry, J. Johnson, K. McDevitt, Effect of cold temperatures on the behavior and ultimate capacity of GFRP-reinforced concrete beams, *Cold Reg. Sci. Technol.* 136 (2017) 9–16.
- [6] S. N. A. B. Safri, M. T. H. Sultan, M. Jawaid, 7 - Damage analysis of glass fiber reinforced composites, in: M. Jawaid, M. Thariq, N. Saba (Eds.), *Durab. Life Predict. Biocomposites, Fibre-Reinforced Compos. Hybrid Compos.*, Woodhead Publishing Series in Composites Science and Engineering, Woodhead Publishing, 2019, pp. 133–147.
- [7] S. Gholizadeh, A review of non-destructive testing methods of composite materials, *Procedia Struct. Integr.* 1 (2016) 50–57.
- [8] L. D. Liu, X. Q. Wu, Defect types and ultrasonic nondestructive testing for fiber-reinforced composites, *Adv. Mater. Res.* 834-836 (2013) 233–236.
- [9] J. Dong, B. Kim, A. Locquet, P. McKeon, N. Declercq, D. S. Citrin, Nondestructive evaluation of forced delamination in glass fiber-reinforced composites by terahertz and ultrasonic waves, *Compos. Part B Eng.* 79 (2015) 667–675.
- [10] E. Cristofani, F. Friederich, S. Wohnsiedler, C. Matheis, J. Jonuscheit, M. Vandewal, R. Beigang, Nondestructive testing potential evaluation of a terahertz frequency-modulated continuous-wave imager for composite materials inspection, *Opt. Eng.* 53 (2014) 031211.
- [11] J. Wang, J. Zhang, T. Chang, H. L. Cui, A Comparative Study of Non-destructive Evaluation of Glass Fiber Reinforced Polymer Composites Using Terahertz, X-ray, and Ultrasound Imaging, *Int. J. Precis. Eng. Manuf.* 20 (2019) 963–972.
- [12] A. Souliman, M. Kahl, D. Stock, M. Möller, B. Engel, P. Haring Bolivar, Defect detection in bi-directional glass fabric reinforced thermoplastics based on 3d thz imaging, preprint (2022).
- [13] R. Yang, Y. He, Optically and non-optically excited thermography for composites: A review, *Infrared Phys. Technol.* 75 (2016) 26–50.
- [14] M. Endrizzi, B. I. Murat, P. Fromme, A. Olivo, Edge-illumination X-ray dark-field imaging for visualising defects in composite structures, *Compos. Struct.* 134 (2015) 895–899.
- [15] M. Endrizzi, P. C. Diemoz, T. P. Millard, J. Louise Jones, R. D. Speller, I. K. Robinson, A. Olivo, Hard X-ray dark-field imaging with incoherent sample illumination, *Appl. Phys. Lett.* 104 (2014).
- [16] M. Endrizzi, A. Olivo, Absorption, refraction and scattering retrieval with an edge-illumination-based imaging setup, *J. Phys. D: Appl. Phys.* 47 (2014).
- [17] A. Olivo, Edge-illumination x-ray phase-contrast imaging, *J. Phys. Condens. Matter* 33 (2021) 363002.
- [18] P. Modregger, T. P. Cremona, C. Benarafa, J. C. Schittny, A. Olivo, M. Endrizzi, Small angle X-ray scattering with edge-illumination, *Sci. Rep.* 6 (2016) 1–8.
- [19] M. Endrizzi, F. A. Vittoria, L. Rigon, D. Dreossi, F. Iacoviello, P. R. Shearing, A. Olivo, X-ray Phase-Contrast Radiography and

- Tomography with a Multiaperture Analyzer, *Phys. Rev. Lett.* 118 (2017) 1–5.
- [20] P. Modregger, M. Kagias, S. C. Irvine, R. Brönnimann, K. Jefimovs, M. Endrizzi, A. Olivo, Interpretation and Utility of the Moments of Small-Angle X-Ray Scattering Distributions, *Phys. Rev. Lett.* 118 (2017) 1–6.
- [21] D. Shoukroun, L. Massimi, M. Endrizzi, D. Bate, S. Olivo, P. Fromme, Composites impact damage detection and characterization using ultrasound and x-ray NDE techniques, *Proc. SPIE* 11381, *Heal. Monit. Struct. Biol. Syst.* XIV (2020) 13.
- [22] D. Shoukroun, L. Massimi, F. Iacoviello, M. Endrizzi, D. Bate, A. Olivo, P. Fromme, Enhanced composite plate impact damage detection and characterisation using X-Ray refraction and scattering contrast combined with ultrasonic imaging, *Compos. Part B Eng.* 181 (2020) 107579.
- [23] D. Shoukroun, L. Massimi, M. Endrizzi, D. Bate, P. Fromme, S. Olivo, Composite porosity characterization using x-ray edge illumination phase contrast and ultrasonic techniques, in: *Heal. Monit. Struct. Biol. Syst.* XV, March 2021, 2021, p. 85. doi:10.1117/12.2582561.
- [24] D. Shoukroun, S. Olivo, P. Fromme, Edge Illumination X-Ray Phase Contrast Imaging and Ultrasonic Attenuation for Porosity Quantification in Composite Structures, *Proc. 2021 48th Annu. Rev. Prog. Quant. Nondestruct. Eval. QNDE 2021* (2021) 1–6.
- [25] F. Pfeiffer, M. Bech, O. Bunk, P. Kraft, E. F. Eikenberry, C. Brönnimann, C. Grünzweig, C. David, Hard-X-ray dark-field imaging using a grating interferometer, *Nat. Mater.* 7 (2008) 134–137.
- [26] F. Pfeiffer, T. Weitkamp, O. Bunk, C. David, Phase retrieval and differential phase-contrast imaging with low-brilliance X-ray sources, *Nat. Phys.* 2 (2006) 258–261.
- [27] T. Thüring, W. C. Barber, Y. Seo, F. Alhassen, J. S. Iwaczyk, M. Stampanoni, Energy resolved X-ray grating interferometry, *Appl. Phys. Lett.* 102 (2013) 10–14.
- [28] A. Sarapata, M. Ruiz-Yaniz, I. Zanette, A. Rack, F. Pfeiffer, J. Herzen, Multi-contrast 3D X-ray imaging of porous and composite materials, *Appl. Phys. Lett.* 106 (2015).
- [29] D. Vavrik, J. Jakubek, I. Jandejsek, F. Krejci, I. Kumpova, J. Zemlicka, Visualization of delamination in composite materials utilizing advanced X-ray imaging techniques, *J. Instrum.* 10 (2015).
- [30] B. Plank, C. Hanneschlaeger, V. Revol, J. Kastner, Characterisation of anisotropic fibre orientation in composites by means of X-ray grating interferometry computed tomography, *Mater. Sci. Forum* 825–826 (2015) 868–875.
- [31] F. Prade, F. Schaff, S. Senck, P. Meyer, J. Mohr, J. Kastner, F. Pfeiffer, Nondestructive characterization of fiber orientation in short fiber reinforced polymer composites with X-ray vector radiography, *NDT E Int.* 86 (2017) 65–72.
- [32] N. Morimoto, K. Kimura, T. Shirai, T. Doki, S. Sano, A. Horiba, K. Kitamura, Talbot-Lau interferometry-based X-ray imaging system with retractable and rotatable gratings for nondestructive testing, *Rev. Sci. Instrum.* 91 (2020).
- [33] F. Röper, B. Plank, J. Glinz, M. Wolfahrt, G. Kucher, G. Pinter, X-ray computed tomography in bonded aircraft repairs for composites, *Proc. 10th Conf. Ind. Comput. Tomogr.* (2020) 1–6.
- [34] S. Wang, T. Yatagawa, H. Suzuki, Y. Ohtake, Image Based Measurement of Individual Fiber Lengths for Randomly Oriented Short Fiber Composites, *J. Nondestruct. Eval.* 41 (2022).
- [35] J. Glinz, M. Thor, J. Schulz, S. Zabler, J. Kastner, S. Senck, Non-destructive characterisation of out-of-plane fibre waviness in carbon fibre reinforced polymers by X-ray dark-field radiography, *Nondestruct. Test. Eval.* 0 (2022) 1–11.
- [36] Y. Kasai, A. Yoshimura, M. Arai, K. Goto, A. Yamanaka, H. Shindo, Relation between dark-field images derived using X-Ray Talbot–Lau interferometer and carbon fiber distribution in CFRP, *Adv. Compos. Mater.* 30 (2021) 591–604.
- [37] J. Kim, A. Slyamov, E. Lauridsen, M. Birkbak, T. Ramos, F. Marone, J. W. Andreasen, M. Stampanoni, M. Kagias, Macroscopic mapping of microscale fibers in freeform injection molded fiber-reinforced composites using X-ray scattering tensor tomography, *Compos. Part B Eng.* 233 (2022) 109634.
- [38] P. C. Diemoz, F. A. Vittoria, A. Olivo, Spatial resolution of edge illumination X-ray phase-contrast imaging, *Opt. Express* 22 (2014) 15514.
- [39] P. C. Diemoz, P. Coan, C. Glaser, A. Bravin, Absorption, refraction and scattering in analyzer-based imaging: comparison of different algorithms, *Opt. Express* 18 (2010) 3494.
- [40] C. Chantler, K. Olsen, R. Dragoset, J. Chang, A. Kishore, S. Kotochigova, D. Zucker, Detailed Tabulation of Atomic Form Factors, Photoelectric Absorption and Scattering Cross Section, and Mass Attenuation Coefficients for $Z = 1-92$ from $E = 1-10$ eV to $E = 0.4-1.0$ MeV, 2005.
- [41] D. Montgomery, Design and Analysis of Experiments, Student solutions manual, John Wiley & Sons, 2008.
- [42] W. H. Press, S. A. Teukolsky, W. T. Vetterling, B. P. Flannery, Numerical Recipes 3rd Edition: The Art of Scientific Computing, 3 ed., Cambridge University Press, 2007.